



LAWRENCE  
LIVERMORE  
NATIONAL  
LABORATORY

# Ordering in Bio-inorganic Hybrid Nanomaterials Probed by In Situ Scanning Transmission X-ray Microscopy

J. R. I. Lee, M. Bagge-Hansen, R. Tunuguntla, K. Kim,  
M. Bangar, T. M. Willey, I. C. Tran, D. Kilcoyne, A. Noy,  
T. van Buuren

October 23, 2014

Nanoscale

## **Disclaimer**

---

This document was prepared as an account of work sponsored by an agency of the United States government. Neither the United States government nor Lawrence Livermore National Security, LLC, nor any of their employees makes any warranty, expressed or implied, or assumes any legal liability or responsibility for the accuracy, completeness, or usefulness of any information, apparatus, product, or process disclosed, or represents that its use would not infringe privately owned rights. Reference herein to any specific commercial product, process, or service by trade name, trademark, manufacturer, or otherwise does not necessarily constitute or imply its endorsement, recommendation, or favoring by the United States government or Lawrence Livermore National Security, LLC. The views and opinions of authors expressed herein do not necessarily state or reflect those of the United States government or Lawrence Livermore National Security, LLC, and shall not be used for advertising or product endorsement purposes.

# Ordering in Bio-inorganic Hybrid Nanomaterials Probed by In Situ Scanning Transmission X-ray Microscopy

Jonathan R. I. Lee,<sup>a</sup> Michael Bagge-Hansen,<sup>a</sup> Ramya Tunuguntla,<sup>a</sup> Kyunghoon Kim,<sup>a,b</sup> Mangesh Bangar,<sup>c</sup> Trevor M. Willey,<sup>a</sup> Ich C. Tran,<sup>a</sup> David A. Kilcoyne,<sup>d</sup> Aleksandr Noy<sup>a</sup> and Tony van Buuren<sup>\*a</sup>

Phospholipid bilayer coated Si nanowires are one-dimensional (1D) composites that provide versatile bio-nanoelectronic functionality via incorporation of a wide variety of biomolecules into the phospholipid matrix. The physiochemical behaviour of the phospholipid bilayer is strongly dependent on its structure and, as a consequence, substantial modelling and experimental efforts have been directed at the structural characterization of supported bilayers and unsupported phospholipid vesicles; nonetheless, the experimental studies conducted to date have exclusively involved volume-averaged techniques, which do not allow for the assignment of spatially resolved structural variations that could critically impact the performance of the 1D phospholipid-Si NW composites. In this manuscript, we use scanning transmission x-ray microscopy (STXM) to probe bond orientation and bilayer thickness as a function of position with a spatial resolution of  $\sim 30\text{nm}$  for  $\Delta 9\text{-Cis}$  1,2-dioleoyl-sn-glycero-3-phosphocholine layers prepared Si NWs. When coupled with small angle x-ray scattering measurements, the STXM data reveal structural motifs of the Si NWs that give rise to multi-bilayer formation and enables assignment of the orientation of specific bonds known to affect the order and rigidity of phospholipid bilayers.

## Introduction

Nature has evolved a set of sophisticated biological machines for accomplishing molecular-level tasks including membrane receptors, channels, and pumps. By combining functional structures from this bio-“toolbox”, such as membrane pore proteins, with the mechanical and electronic properties of novel inorganic nanostructures, a new class of bio-nanoelectronics has emerged that are capable of mimicking and interacting with biological systems.<sup>1</sup> Bio-functionalized nanowires and nanotubes are highly compatible with traditional device architectures and are a leading candidate for both construction of bio-nanoelectronic devices and for integration within living biological systems.<sup>2</sup> Such devices could facilitate sub-cellular bio-sensing for *in vivo* diagnostics<sup>3</sup> and truly biomimetic neuroprosthetics.<sup>4</sup>

Such bio-functionalized nanostructures have been realized via assembly of 1D phospholipid bilayers on carbon nanotubes and silicon nanowires (Si NWs).<sup>5, 6</sup> These biomimetic lipid bilayers shield the nanowire surface from solution interactions and further serve as a general host matrix for bio-functional components such as gateable membrane pore proteins.<sup>7, 8</sup> Fluorescence Recovery After Photobleaching (FRAP) has shown that these 1D lipid bilayers are continuous and maintain adequate fluidity, despite increased strain introduced by accommodating the nanowire curvature (diameter  $\sim 50\text{-}100$

nm).<sup>6</sup> Model bio-nanoelectronic devices have been fabricated by doping these lipid bilayers with membrane pore proteins that act as highly selective ion channels; cyclic voltammetry measurements confirmed that these functional, biomimetic coatings provide a tunable electrochemical interface between inorganic nanostructures and biological systems.<sup>7</sup> Moreover, several nanoelectronic device architectures produced by assembly of bio-functionalized Si NWs into transistor circuits, showed that these devices can detect ion transport through these ion channels as well as voltage-gate the imbedded membrane proteins.<sup>8</sup>

Although significant technological advancement of these materials has been made, fundamental questions remain on the nature of complex structure-function relationships in 1D bilayers. To assess the impact of nanoscale self-organization on device function and to unravel this complex structure-function relationship we need high spatial resolution on the nm-scale, with *in situ* characterization of model bio-nanoelectronic systems. These characterization techniques also need to achieve robust chemical speciation without destroying the samples. Scanning transmission x-ray microscopy (STXM) is uniquely positioned to address these demands.<sup>9</sup> Previous work has shown that C K-edge x-ray absorption spectroscopy (XAS) data derived from STXM images can be used to distinguish and map protein, lipid, polysaccharides, and DNA components in complex microbial biofilms.<sup>10</sup>

$\Delta 9$ -Cis 1,2-dioleoyl-sn-glycero-3-phosphocholine (DOPC) lipid bilayers on Si NWs provide a model hybrid bio-nanostructure system that is well suited for this study as: (1) mature and reproducible synthesis protocols assure the availability of high quality samples, (2) sufficient synthesis flexibility can be used to amplify parameters of interest (e.g., concentration, size, or geometry), and (3) parallel efforts to integrate Si NWs into device architectures suggest this material is a leading candidate for future bio-nanoelectronics applications.

The orientation and structure of DOPC phospholipid layers may be determined by careful examination of angular dependence in the C K-edge XAS, which can be derived from STXM images.<sup>11-13</sup> The XAS resonance intensity of a bond with well-defined orientation varies as a function of the relative orientation of the transition dipole moment and the electric vector of the incident x-ray beam.<sup>14, 15</sup> Analysis of this dichroism can yield the bond and, in many cases, molecular orientation<sup>14, 15</sup>. Identification of any bond orientation within Si nanowire-supported DOPC layers is important in determining the structure of the biofilm; nonetheless, the orientation and degree of order of unsaturated bonds within lipid structures are of particular interest and have been the subject of extensive study, most prominently via simulation, due to their importance in determining the structure and physical properties of the bilayer, including its response to membrane protein or cholesterol insertion. The majority of molecular dynamic (MD) simulations and nuclear magnetic resonance (NMR) studies performed to date indicate that the presence of unsaturated bonds within the hydrophobic chains leads to a substantial reduction in the molecular and segmental (C-H, C-D) order parameters (particularly for carbons within the C=C and vicinal C-C bonds) versus lipids with fully saturated chains;<sup>16-24</sup> even so, higher segmental order parameters were reported for the C=C bonds in MD studies conducted by Rabinovich and co-workers.<sup>25, 26</sup> In addition, several groups suggest that data from experimental NMR and infrared spectroscopy treatments are consistent with the C=C bond axis in DOPC (and 1-palmitoyl-2-oleoyl-sn-glycero-3-phosphocholine, POPC, a structural analogue that has an unsaturated bond in one of the lipid tails) vesicles adopting a well-defined orientation, in which the bond is tilted by  $\leq 10^\circ$  with respect to the bilayer normal.<sup>27-30</sup> Significantly, STXM(XAS) measurements of DOPC on Si NWs offer an excellent opportunity to study the orientation of unsaturated bonds in a supported lipid structure, via analysis of the  $C(1s) \rightarrow \pi^*$  resonance arising from the two isolated C=C bonds within the biomolecule.

In this paper, STXM(XAS) coupled with complementary small angle x-ray scattering (SAXS) measurements are used to determine the coverage and orientation of DOPC lipid layers formed on Si NWs. The SAXS measurements reveal the presence of multi-bilayer lipid structures on the Si NWs, while the STXM data provides sufficient spatial resolution to resolve differences in the thickness of the lipid layer as a function of location on the NW structures. In particular, the Si NWs are shown to be covered with a layer of DOPC lipids, in principle as thin as a single bilayer, which substantially thickens at contact points between the NWs, potentially due to disruption of the liposome fusion process. In addition, analysis of angular dependent XAS spectra derived from the STXM images indicates that the C=C bonds within the hydrophobic tails of DOPC do, indeed, have a statistically averaged preferred

orientation, which is discussed in reference to prior MD modelling and NMR studies.

## Results and discussion

Fig. 1 displays SAXS profiles of bare and 18:1  $\Delta 9$ -Cis 1,2-DOPC coated Si NWs, prepared using nominally 100 nm diameter DOPC liposomes. Inspection of the SAXS profiles reveals pronounced differences, starting from  $q \sim 0.05 \text{ \AA}^{-1}$  upon coating of the Si NWs with DOPC. Two lobes are clearly resolved in the SAXS profile of the DOPC-coated Si NWs, at  $q \sim 0.15$  and  $0.35 \text{ \AA}^{-1}$ , that are not observed in the profile of the bare Si NWs. These features are consistent with the characteristic scattering profile observed for free DOPC vesicles in aqueous solution and, therefore, are attributed to the presence of DOPC layers on the surface of the Si NWs.<sup>31</sup>

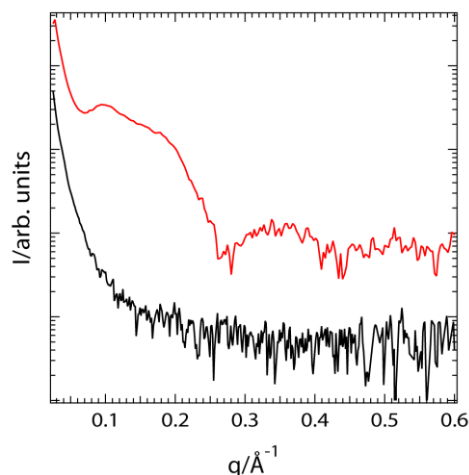


**Fig. 1** SAXS profiles of bare Si NWs (black), and DOPC coated Si NWs prepared using 100 nm diameter liposomes (red). The profiles are offset vertically for clarity.

The SAXS profile for the DOPC coated NWs exhibits some apparent asymmetry in the lobe at  $\sim 0.15 \text{ \AA}^{-1}$ , which arises due to the presence of two sharp, superimposed, features at  $\sim 0.1$  and  $0.2 \text{ \AA}^{-1}$  respectively. These sharp features are characteristic of first and second order Bragg diffraction attributed to the presence of multi-lamellar structures.<sup>32</sup> The formation of multi-bilayer (pauci-lamellar or multi-lamellar) structures is known to occur for zwitterionic lipids such as DOPC because of the attractive interactions between the outermost surfaces of neighbouring bilayers.<sup>33</sup> Significantly, the diffraction peaks present in the volume-averaged SAXS data do not enable identification of any spatial variation in the thickness of the DOPC layer as a function of position on the Si NWs. The SAXS results pose important questions regarding the structure of the DOPC/Si NW system that are crucial to understanding the function and performance of the lipid layer: (1) is the DOPC layer of uniform thickness at all points on the Si NWs?, (2) are regions of distinct thickness randomly distributed on the NWs or do they adopt a well-defined spatial arrangement?, and (3) do regions of a particular thickness exhibit any characteristic structural features or distinct chemistry? STXM is ideally suited to address these questions because it provides the spatial resolution to study individual wires while also offering the electronic structure and bonding information available from analysis of the XAS derived from energy stacks of STXM images (see experimental section).

Figs. 2(a) and (b) display *in situ* STXM images collected on beamline BL5.3.2.1 of the Advanced Light Source (ALS) for DOPC-coated Si NWs at energies immediately below (1830 eV) and above (1850 eV) the Si *K*-edge (1839 eV). Extended clusters composed of rod-like features are observed in Fig. 2(b) that have the characteristic dimensions of the Si NWs (diameters of 50-100 nm and lengths up to several  $\mu\text{m}$ ); in contrast, Fig. 2(a) is devoid of any comparable features, indicating that the structures observed in Fig. 2(b) exhibit dramatically increased photon absorption at energies above the Si *K*-edge and, therefore, must be Si-based. These features of the images in Fig. 2 indicate that the observed structures are Si NWs and definitively demonstrate that high spatial resolution imaging is possible within the aqueous environment of our *in situ* cells. We note that a relative intensity map (see Supporting Information) derived from the images displayed in Figs. 2(a) and (b) provides additional support that the rod-like features are Si NWs.

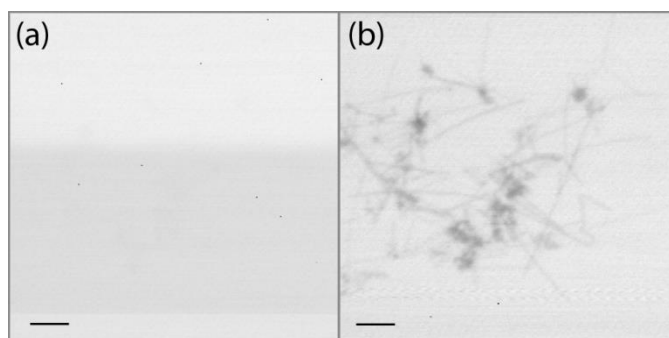


**Fig. 2** Sequentially recorded STXM images for a specific region of DOPC-coated Si NWs under an aqueous environment within an *in situ* cell at (a)  $h\nu = 1830$  eV and (b)  $h\nu = 1850$  eV. The scale bars correspond to 1  $\mu\text{m}$ .

Si NWs are also readily resolved in STXM images recorded at energies that encompass the C *K*-edge, which is illustrated by Fig. 3. The *in situ* STXM images in Figs. 3(a) and (b) are representative of data collected for DOPC-coated Si NWs in  $\text{H}_2\text{O}$  at energies below (280 eV) and above (300 eV) the C *K*-edge. Both exhibit characteristic features of the Si NWs, specifically rod-like structures in branching arrangements comparable with those displayed in Fig. 2(b). The observation of Si NWs at energies close to the C *K*-edge (Figs. 3(a) and (b)) but not at energies immediately below the Si *K*-edge (Fig. 2(a)) is anticipated from the relative photon attenuation lengths in Si. At 1830 eV, the photon attenuation length exceeds 14  $\mu\text{m}$  and, therefore, the  $\sim 100$  nm diameter nanowires do not sufficiently attenuate the x-ray beam to yield observable contrast in the images recorded at this energy; meanwhile, the photon attenuation lengths at 280 and 300 eV (116 and 133 nm respectively)<sup>34-36</sup> are comparable with the Si NW diameter and result in substantial contrast between the NWs and the surrounding solution in the STXM images.

Relative intensity mapping (see Supporting Information) of the data displayed in Figs. 3(a) and (b) reveals a significant increase in contrast between the Si NW features and the surrounding solution as the photon energy is increased from 280 to 300 eV. This increase in contrast cannot arise solely from attenuation by the Si NWs because water exhibits a greater proportional increase in photon attenuation length over the 280-300 eV energy range (19% vs. 15% for  $\text{H}_2\text{O}$  vs. Si).<sup>34-36</sup> Bare wires would exhibit a subtle decrease in contrast between

the Si NW and the surrounding  $\text{H}_2\text{O}$  as the photon energy is increased from 280 to 300 eV, which is in direct contradiction to the measurement. The increase in contrast thus arises due to the presence of a carbon-based coating on the surfaces of the Si NWs. The assignment of a carbon-based coating on the NW surfaces is supported by STXM images recorded at 280 and 300 eV (Figs. 3(c) and (d) respectively) for uncoated Si NWs (i.e. in the absence of DOPC, Fig. 3(e)) in water, which exhibit no comparable increase in contrast (see also the relative intensity map provided in the Supporting Information).

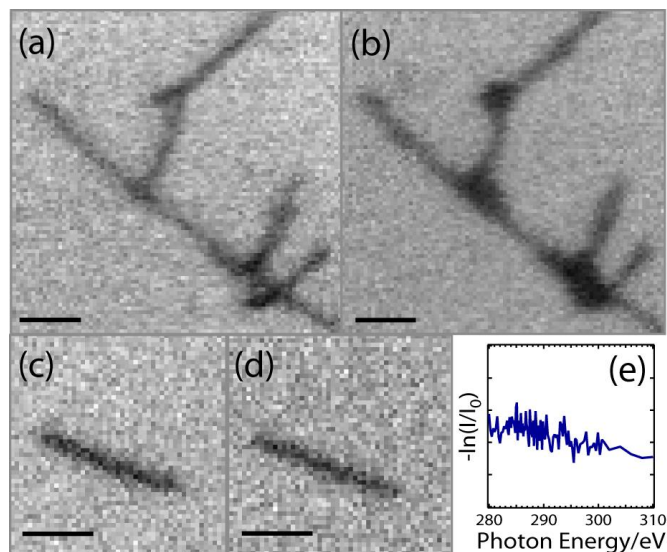


**Fig. 3** Sequentially recorded STXM images for a specific region of DOPC-coated Si NWs under aqueous environment within an *in situ* cell at (a) 280 and (b) 300 eV. Corresponding STXM images recorded at (c) 280 and (d) 300 eV for a Si NW under aqueous environment in the absence of DOPC. The scale bars in (a) through (d) correspond to 400 nm. (e) Carbon *K*-edge XAS data obtained from analysis of the ‘stack’ encompassing (c) and (d).

Further inspection of Figs. 3(a) and (b) reveal that the increase in contrast (and apparent NW dimensions) between 280 and 300 eV varies as a function of position on the Si NWs. In particular, analysis of these data (see SI) suggests that substantially more carbon ( $3.8 \pm 0.3$  times thicker) is found at wire nodes (i.e. at points where two distinct NWs meet) than on regions of the wire that are separated from these junctions. This node-localized increase in carbon is nearly twice as much as would be expected from a simple superposition of two uniformly coated Si NWs. We speculate that the multi-bilayer signal observed in the SAXS data arises, at least in part, from the thicker lipid coating observed at the nodes. It is possible that the nanowire geometry around the nodes disrupt the liposome fusion process and produces multilayered structures. This hypothesis necessitates verification that the carbon-based layer identified in the STXM images arises from the presence of surface-attached DOPC molecules, rather than other carbonaceous contaminants preferentially adsorbed on the NWs. Such validation of the presence of DOPC on the NW surfaces is achieved via the analysis of X-ray absorption spectra derived from STXM energy stacks over the carbon *K*-edge.

Fig. 4(a) displays carbon *K*-edge XAS data obtained from representative energy stacks recorded within a single experimental sample, which contained four Si NWs of distinct orientations. Each orientation is defined with respect to a Cartesian coordinate scheme (contained within Fig. 4(b)) in

which the NWs (and the cell windows) reside in the x-y plane, with the axis of the x-ray beam along the z-axis. The angle of each nanowire,  $\alpha$ , is measured with respect to the x-axis, which is coincident with the electric vector of the incident radiation (**E**). Images for each NW orientation, recorded at 300 eV within the respective stacks, are displayed in Figs. 4(b) through (e). A carbon K-edge XAS spectrum derived from an energy stack recorded for unbound DOPC liposomes under aqueous solution is also included in Fig. 4(a) for the purposes of direct comparison. Inspection of Fig. 4(a) reveals that the XAS spectra obtained from the lipid-coated Si NWs exhibit the same resonances and general appearance observed for DOPC in solution and reported for ex situ XAS measurements of dry DOPC.<sup>37</sup> In particular, the resonances at  $\sim 285.2$  and  $\sim 288$  eV (I and II respectively) arise from  $\pi^*$  resonances of the C=C<sup>37-41</sup> and C=O (ester)<sup>37, 39-42</sup> bonds present in each hydrophobic tail of the DOPC, the low intensity resonance resolved at  $\sim 290$  eV (III) is attributed to C-H  $\sigma^*/R^*$  resonances,<sup>37</sup> and features at higher energies (IV) are assigned to a series of C-C and C-O  $\sigma^*$  resonances.<sup>37</sup> Such close similarity between the XAS for the lipid-coated Si NWs and unbound DOPC liposomes provides evidence that the carbon-based layer on the surface of the Si NWs is indeed composed of DOPC lipids.

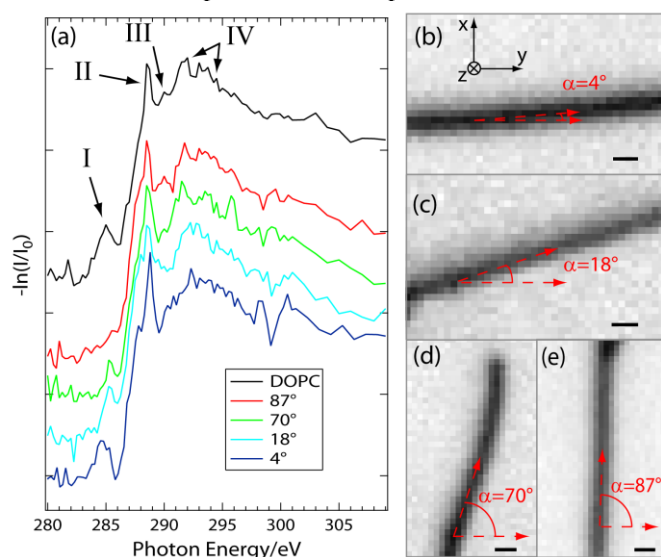


**Fig. 4** (a) Carbon K-edge XAS spectra obtained via analysis of STXM ‘stacks’ collected under *in situ*, aqueous, conditions for DOPC vesicles, and DOPC-coated Si NWs of distinct orientations. Representative STXM images recorded at 300 eV and extracted from the ‘stacks’ used to generate the XAS spectra presented in (a) are displayed in (b) through (e). The scale bars in (b) through (e) correspond to 100 nm and (b) contains a schematic of the Cartesian coordinate scheme.

Given that the SAXS data indicate the presence of multi-bilayer films of different thicknesses, Figs. 3 and 4 also demonstrate that our STXM measurements offer the sensitivity to distinguish between and selectively probe regions of distinct lipid layer thicknesses, potentially down to a single bilayer, via analysis of the transmitted beam intensity. For the DOPC on Si NW system, this capability is of practical importance in guiding device assembly because it reinforces that one must avoid the use of branched or node-containing NWs in an integrated circuit. Structural inhomogeneities at the nodes could potentially cause two problems: (1) selective, membrane protein-mediated, ion transport channels might not be available

through multi-bilayer arrangements or, alternatively, (2) disruption of the fusion process could lead to structural defects in the phospholipid layer that permit undesirable ion transport pathways to the Si NW which would be detrimental to the device performance. The capability to monitor the thickness of the phospholipid layer also provides a means to evaluate sample preparation before using the coated Si NWs in a device.

Although the XAS data extracted for the four Si NWs exhibit strong similarities in appearance, the intensity of the C=C  $\pi^*$  resonance evolves as a function of the NW orientation (fig 4(a)). The C=C  $\pi^*$  resonance intensity is substantially diminished at the highest angle ( $\alpha = 87^\circ$ ) and then systematically increases as a function of decreasing  $\alpha$ . Angular dependence in the C=C  $\pi^*$  resonance intensity indicates that the C=C bonds adopt a preferred, statistically averaged, orientation within the DOPC layer on Si NW surfaces. The assignment of a preferred orientation for the C=C  $\pi$ -bond from the XAS spectra presented in Fig. 4(a) is possible because the intensity of an XAS resonance is proportional to the dot product of **E** and the transition dipole moment vector (TDMV) of the orbital into which the electron is promoted during X-ray absorption<sup>14, 15</sup>. Hence, the intensity of the C=C  $\pi^*$  resonance can only change if (1) the C=C  $\pi$ -bonds adopt a specific (statistically averaged) orientation on the Si NWs within the DOPC layer and (2) **E** is highly polarized in a particular plane. If conditions (1) and (2) are both fulfilled, rotating the Si NWs in the x-y plane alters the angle between the  $\pi$ -bonds and **E** and changes in intensity will result. Significantly, **E** on bend magnet beamline BL5.3.2.2 exhibits a high degree of linear polarization ( $89 \pm 6\%$  in the plane of the synchrotron storage ring on BL5.3.2.2<sup>43</sup>) and, therefore, the data indicate that the C=C bonds must adopt a preferential orientation when the DOPC monomers form a layered structure on the Si NWs.

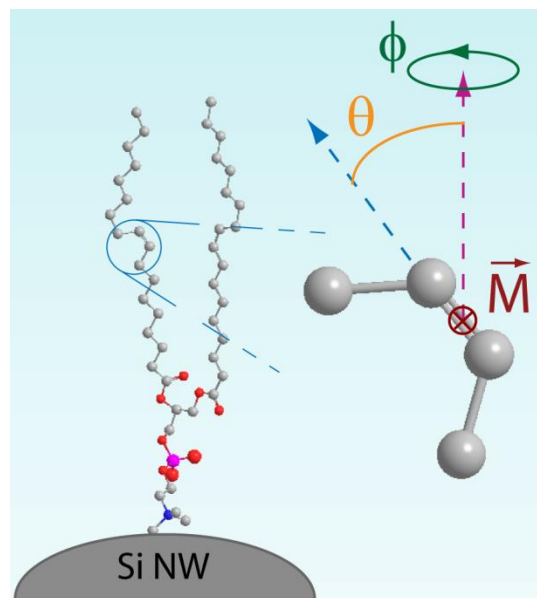


**Fig. 5** Schematic (not to scale) indicating the tilt (polar,  $\theta$ ) and twist (azimuthal,  $\phi$ ) angles for a C=C bond within one of the hydrophobic tails of DOPC. The same co-ordinate scheme is used to define the orientation of all double bonds in the DOPC molecule, including the C=O bond of the ester grouping within the same tail and the C=C and C=O bonds in the second hydrophobic tail. Individual atoms are denoted by filled spheres with the following colours: carbon, gray; oxygen, red; nitrogen, blue; and phosphorous, pink (hydrogen atoms are omitted for clarity). The purple arrow is coincident with the



surface normal at the point of contact between the DOPC and the Si NW, the dark red arrow corresponds to the TDMV, (**M**) for the  $\pi^*$ -orbital of the C=C bond (or the C=O bond of the ester group) and the blue arrow is coincident with the C=C bond. Note that, in principle, each double bond is free to adopt a distinct orientation from all of the others.

Linear regression analysis of the intensity variations of an XAS resonance as a function of  $\alpha$  can provide a quantitative measurement of the orientation adopted by the associated bond. This methodology is described extensively within the literature<sup>14, 15, 44, 45</sup> and has been used to great effect in the study of many materials systems, particularly thin organic films assembled on a variety of planar substrates. Such analyses can be extended to the DOPC-coating on Si NW surfaces via a qualitative treatment of the trend in intensity variation of the C=C  $\pi^*$  resonance as a function of  $\alpha$ , which would provide valuable insight into the structure of the DOPC that cannot be obtained by alternative characterization techniques. We note that the changes in the C=C  $\pi^*$  resonance intensity, and the XAS spectra as a whole, are not consistent with substantial beam damage (see discussion in the Supporting Information), which is an important consideration when studying organic/biomolecules with STXM.<sup>46, 47</sup>

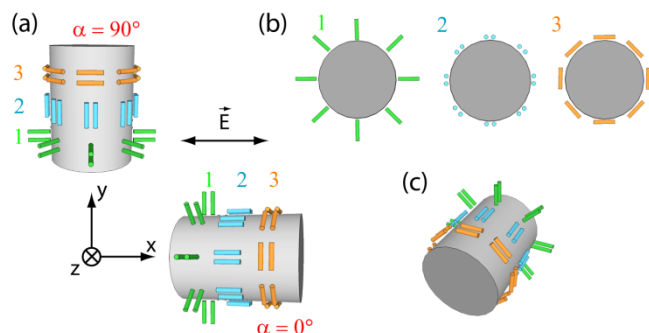


**Fig. 6** Schematics (not to scale) illustrating three limiting cases for the orientation of a C=C or C=O double bond within DOPC molecules attached to the surface of Si NWs. Equivalent orientations of the double bonds are denoted as follows: 1 (green), the axis of the double bond is coincident with the surface normal of the Si NW; 2 (light blue), the axis of the double bond lies perpendicular to the surface normal of the Si NW and is co-linear with the long axis of the NW; 3 (orange), the axis of the double bond lies perpendicular to both the surface normal and long axis of the Si NW. The schematic displayed in (a) corresponds to the orientation of a STXM image, in which the Si NWs reside in the xy plane (specifically along the x- and y-axes in this instance) and are viewed along the axis of the incident x-ray beam (the z-axis). Note that the electric vector of the x-ray beam (**E**) is co-linear with the x-axis and the Si NWs are slightly tilted in the z-direction to add perspective. Schematics (b) and (c) are included to provide additional perspective regarding the relative orientation between the double bonds and Si NW for each limiting case. In (b) the Si NWs are viewed end on (i.e. along the long axis of the NW) and in (c) the long axis of the Si NW is oriented at  $\sim 45^\circ$  to all three axes.

The orientation of the C=C  $\pi^*$  TDMV with respect to (1) the C-C (or C-O) axis and (2) the Si NW surface are illustrated by the schematic in Fig. 5. The TDMV (**M**) lies perpendicular to the plane formed by the C-C=C-C moiety and, therefore, will follow any reorientation of the C=C bond. The orientation of the TDMV with respect to the Si NW is defined using a polar

co-ordinate scheme in which the polar ( $\theta$ ) and azimuthal ( $\phi$ ) angles are measured relative to the Si surface normal at the point of contact between the DOPC and the NW. Within this scheme, it is assumed that free rotation around the C=C axis is possible via rotation of the hydrocarbon chains of the DOPC. Significantly, one cannot devolve  $\theta$  from  $\phi$  via measurement with a single x-ray source, even for data with signal-to-noise suitable for quantitative analysis, because this process requires the ability to characterize two degrees of freedom and the XAS (STXM) measurements with fixed **E** and fixed x-y sample planes yield only one. By defining the orientation of the  $\pi^*$  TDMV using a co-ordinate scheme based upon the Si surface normal at the point of contact between the NW and lipid, it is evident that the values of  $\theta$  and  $\phi$  will remain constant for a well-defined orientation of the C=C (or C=O) bond, irrespective of the location of a DOPC monomer with respect to the NW, i.e. at any point on the circumference of the NW or displaced vertically from the NW surface (as is the case for a C=C bond within a hydrophobic tail of the lipid). Nonetheless, the orientation of the TDMV of the C=C bond with respect to **E** can change appreciably as a function of the position of the DOPC monomer on the Si NW surface (Fig. 6).

Identifying the orientation(s) of the C=C bond that are consistent with trends observed in the XAS data can be achieved by modelling and then comparing the resonances intensities for all possible combinations of  $\theta$  and  $\phi$  at all points on the curved surface of a Si NW. Nevertheless, we first consider a series of limiting cases (illustrated schematically in Fig. 6) for orientations of both the C=C bond and the Si NW given that, experimentally, **E** lies along the x-axis. Three orientations of the axis of the C=C bond are considered: (1) aligned with the surface normal of the Si NW, (2) perpendicular to the surface normal but aligned with the long axis of the Si NW, and (3) perpendicular to both the Si surface normal and the long axis of the NW. These three orientations are coupled with two distinct Si NW orientations to monitor how the C=C  $\pi^*$ -resonance intensity would evolve as the NW rotates in the x-y plane: (i) with the long axis of the Si NW aligned with the x-axis ( $\alpha = 0^\circ$ ), i.e. aligned with **E**, and (ii) aligned with the y-axis ( $\alpha = 90^\circ$ ), i.e. perpendicular to **E**.

We begin by considering C=C bond orientation (1) and qualitatively addressing the evolution in the C=C  $\pi^*$ -resonance intensity with Si NW rotation from  $\alpha = 0^\circ$  to  $\alpha = 90^\circ$ . For  $\alpha = 0^\circ$ , the axis of the C=C bond located on the uppermost surface of the Si NW lies perpendicular to the x-axis. As a consequence, the TDMV of the  $\pi^*$ -orbital is coincident with **E** and the resonance intensity for this C=C bond will be a maximum. As one moves around the circumference of the NW, from the uppermost position to the side of the NW, it is apparent that all of the C=C bonds for orientation (1) are perpendicular to the x-axis. Therefore, all of the bonds provide the maximum resonance intensity and, overall, bond orientation (1) coupled with an NW orientation of  $\alpha = 0^\circ$ , will yield the absolute maximum  $\pi^*$  resonance strength. A reduction in intensity is encountered for C=C bond orientation (1) when the NW is rotated from  $\alpha = 0^\circ$  to  $\alpha = 90^\circ$ . The axis of the C=C bond located on the uppermost surface of the Si NW remains perpendicular to the x-axis and, as such, will retain the maximum resonance strength, while C=C bonds at the side of the NW, co-linear to the x-axis, have TDMV's perpendicular to **E** and, therefore, do not contribute to the resonance intensity. The result of the reduction in signal intensity between C=C bonds located on the uppermost surface and the side of the NW will be a combined  $\pi^*$ -resonance of intermediate intensity for

C=C bonds in orientation (1) on NWs at  $\alpha = 90^\circ$ . Overall, the resonance intensity for C=C bond orientation (1) will reduce as the Si NW rotates from  $\alpha = 0^\circ$  to  $\alpha = 90^\circ$ , which is consistent with the experimental XAS data.

Bond orientation (2) exhibits contrasting behavior to (1). Irrespective of the position on the circumference of the Si NW at  $\alpha = 0^\circ$ , the axis of the C=C bond resides co-linear with the x-axis. As such, the TDMV always resides perpendicular to  $\underline{E}$  and the overall  $\pi^*$  resonance intensity will be at a minimum. With bond orientation (2) and the Si NW at  $\alpha = 90^\circ$ , this situation is reversed – all of the C=C bonds are now perpendicular to the x-axis, the corresponding TDMVs are aligned with  $\underline{E}$  and the overall signal will be at a maximum. Therefore, there will be a considerable increase in the overall resonance intensity upon rotation of the Si NW from  $\alpha = 0^\circ$  to  $\alpha = 90^\circ$  for C=C bond orientation (2), which is inconsistent with the experimental data.

Finally, we consider C=C bond orientation (3). For Si NWs at  $\alpha = 0^\circ$  the axis of the C=C bond is perpendicular to the x-axis, irrespective of the location of the bond on the circumference of the NW. As a consequence, the TDMV is always aligned with  $\underline{E}$  and the overall  $\pi^*$ -resonance intensity will be a maximum. For NWs at  $\alpha = 90^\circ$ , the TDMV of C=C bonds on top of the NW is co-linear with  $\underline{E}$ , whereas a C=C bond at the side of the NW has a TDMV perpendicular to  $\underline{E}$ . This leads to an intermediate overall resonance intensity for NWs at  $\alpha = 90^\circ$  and, by extension, a reduction in intensity vs. Si NWs at  $\alpha = 0^\circ$ . Hence, bond orientation (3) is also qualitatively consistent with the experimental data.

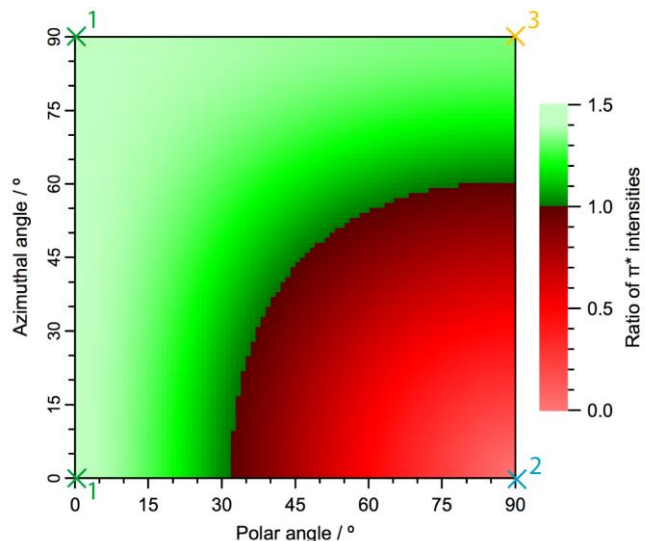


**Fig. 7** Graph of the C(1s)  $\rightarrow \pi^*$  resonance intensity ratio over all possible combinations of polar and azimuthal angle for the C=C bond (or, indeed, the C=O bond) for an Si NW with the long axis aligned with the x-axis (i.e. parallel to  $\underline{E}$ ) versus alignment with the y-axis (i.e. perpendicular to  $\underline{E}$ ). For reference, orientations 1, 2, and 3 from figure 6 are marked on the graph. A full description of the model calculated to generate this graph is included in the supporting information. Note, however, that the model accounts for signal attenuation by the Si NW. The limiting cases described in the text and displayed in figure 6 are marked with crosses of the corresponding colours on the graph. Since orientation 1 is invariant with rotation in  $\phi$ , it can be described by any point along the y-axis (i.e. at  $\theta = 0^\circ$ )

Treatment of the three limiting cases indicates that two of them, specifically (1) and (3), exhibit behaviour consistent with the angular dependence observed experimentally for the  $\pi^*$  intensities, i.e. stronger for NWs at  $\alpha = 0^\circ$  and weaker for NWs at  $\alpha = 90^\circ$ . A thorough analysis of every possible combination of  $\theta$  and  $\phi$  indicates that orientations related to (1) and (3) actually account for all C=C bond orientations that are consistent with the experimental data. Fig. 7 displays a graph of the ratio of C=C  $\pi^*$  resonance intensities for Si NW orientations  $\alpha = 0^\circ$  vs.  $\alpha = 90^\circ$  at each combination of  $\theta$  and  $\phi$ . Inspection of this graph reveals that ratios large enough to be observed above the noise envelope of the experimental data are oriented with polar angles close to  $\theta = 0^\circ$  (C=C bond axis aligned with the Si surface normal, orientation (1)) and/or azimuthal angles close to  $\phi = 90^\circ$  (C=C bond axis perpendicular to the long axis of the Si NW, orientation (3)). At  $\theta = 0^\circ$ , variation in  $\phi$  serves to rotate the TDMV about the Si surface normal, but the axis of the C=C bond remains aligned with the surface normal (although the orientation of the surrounding C-C bonds can change dramatically). Even for non-zero polar angles close to  $\theta = 0^\circ$ , variation in  $\phi$  brings about only small changes in the orientation of the C=C axis, which remains largely upright. In contrast, substantial changes in orientation accompany variation in  $\theta$  for  $\phi = 90^\circ$ : as  $\theta$  increases, the C=C axis rotates from orientation (1) to orientation (3), remaining orthogonal to the long axis of the Si NW at all times (non-zero azimuthal angles will result in minor deviations from this orthogonal arrangement).

The viable combinations of  $\theta$  and  $\phi$  are a limited subset of all possible C=C bond orientations. Further discrimination between the orientations within this subset is desirable and cannot be achieved via analysis of the XAS in isolation. Instead, comparison with the literature provides additional insight and a strong indication that the C=C bond resides closer to orientation (1) than orientation (3). Molecular dynamics simulations and a series of experimental techniques used to evaluate total bilayer (or, in some cases, individual leaflet) thicknesses demonstrate that the overall orientation of DOPC monomers both with and without a substrate support reside more upright than prostrate with respect to the bilayer normal. Although the overall monomer orientation does not indicate the orientation of individual bonds, it does suggest that a prostrate orientation of the C=C bonds could necessitate gauche defects within the hydrophobic chains to retain an overall upright configuration and/or that portions of the hydrophobic chains would protrude laterally (i.e. perpendicular to the surface normal). In either event, the prostrate C=C bond would represent a discontinuity in the pseudo-linear arrangement of the hydrophobic chains, which would lead to less favorable Van der Waals packing interactions (undesirable steric effects) between chains within the same monomer and, more importantly, neighboring monomers within the layer. Indeed, several MD studies that account for the orientation of individual bond orientations assign more upright than prostrate orientations of the C=C axis, including the research of Rabinovich *et al.* that predicts the C=C bonds in monounsaturated hydrophobic chains will adopt polar angles  $\geq 10^\circ$  closer ( $\theta \sim 20^\circ$ ) to the bilayer normal than any of the C-C bonds within the same chain (or within a completely saturated chain).<sup>25</sup> Experimental studies of self-assembled monolayers (SAMs) prepared from organothiol monomers on metal substrates, which serve as simplified structural analogues of the lipid chains and whose packing is heavily influenced by Van der Waals interactions, also indicate a strong preference for the



polar angle of any C=C bonds to reside close to the surface normal.<sup>48</sup> Hence, we propose that a preponderance of the C=C double bonds within the DOPC layers on Si NWs are oriented more upright (closer to the Si surface normal) than prostrate and, importantly, that deviation in the polar angle from  $\theta = 0^\circ$  is generally in the direction of  $\phi = 90^\circ$  (i.e. perpendicular to the long axis of the Si NW). It is noteworthy that this assignment is consistent with the C=C orientations derived via comparison of NMR and infrared spectroscopy data for unsupported membranes prepared from DOPC (and POPC).<sup>27-30</sup>

The assignment of a well-defined DOPC C=C bond orientation provides a valuable reference point for structural modeling of supported phospholipid bilayers and their response to membrane protein insertion. Evidence of ordering in the DOPC layers also has potentially important implications for aspects of their function. In particular, comparison with the behavior of SAMs<sup>49, 50</sup> suggests that layers with ordered molecular packing present a more effective barrier to ion transport, which is a central function of the DOPC for bionanoelectronic applications – ion transport is desired only through specific membrane proteins inserted in the phospholipid layer.

Further inspection of Fig. 4(a) indicates that, in contrast to the C=C  $\pi^*$ -resonance, neither the C=O  $\pi^*$  resonance nor C-C  $\sigma^*$  resonances exhibit any angular dependent intensity changes above the S/N. The absence of any appreciable angular dependence in the C-C  $\sigma^*$  resonance intensities is consistent with the both the molecular and segmental order parameters identified via both MD simulations and NMR studies of free-standing bilayers composed of lipids containing monounsaturated hydrocarbon chains. The overall loss in order within the chains as a function of distance from the hydrophilic headgroup, combined with the extensive disruption in order induced by the presence of the C=C bond with respect to fully saturated chains, would be expected to yield a broad range of C-C orientations. While this range is unlikely to represent a truly random distribution, the deviations from a specific, well-defined, C-C orientation will be sufficient to preclude the observation or assignment of any trend in the associated resonance intensities as a function of NW orientation.

Two phenomena provide the most probable explanations for the lack of angular dependence for the C=O  $\pi^*$  resonance. First, there is insufficient order among the C=O bonds to observe any dichroism in the XAS signal. Second, the C=O bonds adopt a well-defined orientation with respect to both the NW axis and surface normal but the combination of  $\theta$  and  $\phi$  falls in a region where there is limited variation in the resonance intensity as a function of  $\alpha$ ; consequently, the angular dependence would be lost within the S/N. In contrast to the analysis of the C=C bond orientation, comparison with the literature provides limited assistance in distinguishing between these explanations for the arrangement of C=O bonds. MD simulations and NMR experiments do not provide specific evidence of ordering among the C=O bonds, yet the associated segmental order parameters are substantially higher than for the C=C bonds, which preserves the possibility that the C=O bonds exhibit a well-defined, statistically averaged, orientation (or symmetry related orientations).

## Experimental

### Sample Preparation

All DOPC lipids used in this study were obtained from Avanti Polar Lipids. DOPC liposomes were prepared in aqueous

solutions at concentrations of 15, 20, or 30 mg/mL, via hydration of the lipid films with deionized water for 30 minutes at room temperature. To ensure formation of unilamellar liposomes, the samples underwent 10 cycles of freeze/thaw in liquid nitrogen and extrusion through 50, 100, or 200 nm pore diameter polycarbonate membranes (Avanti Polar Lipids), depending on the desired liposome size.

A silicon oxide on silicon growth wafer (1 cm x 1 cm) containing Si NWs grown by chemical vapor deposition was immersed into the liposome solution and bath-sonicated in short 3-second pulses for approximately 60 s to release the wires from the growth substrate. After achieving a dark-brown coloured solution, the piece(s) of silicon oxide on silicon wafer were removed and the liposome-NW solution was transferred to a fresh 1 mL vial. This solution vial was then placed on a slow rocker at room temperature for 12 hours to allow complete liposome fusion onto the Si NWs to create a continuous coating on the wires. The lipid-coated Si NWs were subsequently centrifuged on a table-top centrifuge at low speeds (~3000 rpm) for 90 sec to form a loose pellet of the Si NWs at the bottom of the vial. Most of the supernatant was removed without disturbing the pellet or drying out the Si NWs completely. The pellet was then resuspended in 400  $\mu$ L of water with gentle mixing. This step was conducted to remove unbound free-floating vesicles in solution and repeated 6-10 times with the aim of yielding a final solution of lipid-coated Si NWs containing minimal unbound DOPC, which would otherwise provide an overwhelming contribution to the overall STXM signal.

In preparation for in situ STXM measurements, the aqueous solutions of DOPC on Si NWs were exposed to ~ 30 s of ultra-sonication to disperse the DOPC-coated Si NWs and ~ 1  $\mu$ L was immediately trapped between two Si wafers, each containing a thin (75nm) SiN<sub>x</sub> membrane (25 x 25  $\mu$ m, Silson Ltd or Norcada Inc.). The edges of the two wafers were then bonded together with Torr Seal to yield a hermetically sealed cell, thereby ensuring that the DOPC-coated NWs remained under an aqueous environment even during exposure to the vacuum conditions (or low pressure He<sub>(g)</sub> environment) required for STXM measurements. Significantly, the membranes within the two wafers were aligned (surface tension forces typically result in self-alignment of the two wafers) prior to sealing to ensure that the cell contained a path of minimum x-ray attenuation for the purposes of imaging the experimental sample. STXM measurements were also conducted for a series of experimental standards that included aqueous solutions of (i) DOPC-free Si NWs and (ii) DOPC vesicles.

### Instrumentation and data analysis protocols

All STXM measurements were performed on bend magnet BLs 5.3.2.1 and 5.3.2.2 of the ALS, Lawrence Berkeley National Laboratory (LBNL).<sup>51</sup> Each beamline employs a spherical-grating monochromator to select x-ray photons in the energy ranges of 350-2,500 eV and 250-800eV respectively, with energy resolutions of ~ 0.1eV. Focusing of the monochromatic x-ray beam onto the experimental sample is achieved using a Fresnel zone plate lens; in addition, a scintillator-multiplier assembly located behind the sample is used to detect transmitted photons. Image contrast is provided by differences in the intensity of the transmitted photons as a function of position in the experimental sample and, therefore, is dependent upon the processes of photon absorption during photoexcitation of core electrons within specific elements. A 2D image is recorded at a single photon energy by interferometer-controlled

scanning of the sample in the plane perpendicular to the axis of the incident beam. During the course of this study, images were collected at a spatial resolution of  $\sim 31$  nm and image sequences ('energy stacks') were recorded over a spectral range of 275-330 eV to enable extraction and analysis of carbon K-edge XAS data.

Image alignment and extraction of the transmitted intensities for pixels in a given region of interest within each stack were performed using aXis2000. In the absence of a capability to measure an  $I_0$  signal prior to the sample, the transmitted intensity through an unmodified  $\text{SiN}_x$  membrane was used to account for variations in the intensity of the incident flux as a function of energy. This approach does not enable an absolute measurement of the XAS for DOPC-coated Si NWs because the intensity transmitted through the window does not account for the signal from any free DOPC vesicles remaining in solution; nonetheless, it does account for absorption by the  $\text{SiN}_x$  windows and, more importantly, any carbonaceous species adsorbed on the windows prior to cell assembly (i.e. during fabrication and subsequent storage). Moreover, the washing steps ensure that the remnant amount of free DOPC is low and, at a fixed DOPC concentration, the associated contribution to the overall XAS signal will be constant as a function of position within a specific cell. A position-independent, low level, contribution to the XAS would also be expected if a layer of DOPC adsorbed onto the  $\text{SiN}_x$  windows. Therefore, any differences in the XAS signals obtained from independent wires or between a wire and the surrounding solution are directly attributable to differences in the DOPC adsorbed onto the surface of the Si NWs.

SAXS experiments were performed at the Bio-SAXS beamline 4-2 of the Stanford Synchrotron Radiation Lightsource<sup>52</sup> using a slit-collimated monochromatic X-ray beam with a beam size of  $0.2 \times 0.2$  mm (FWHM) and an X-ray energy of 11 keV (wavelength  $1.1271\text{\AA}$ ). Solution samples of unbound liposomes and liposomes coated on Si NWs in water (with a total volume of  $30\text{ }\mu\text{L}$ ) were handled by an automatic sample changer system<sup>52</sup> that includes loading samples from individual sample microtubes on a temperature-controlled sample rack, injecting samples by a syringe needle into an open-end quartz capillary ( $10\text{ }\mu\text{m}$ -thick walls,  $1.5$  mm diameter) set vertically in-line of the X-ray beam, and unloading samples after the measurements. The needle and capillary was thoroughly flushed and cleaned of irradiated sample by using pure water and different cleaning solutions, and dried by compressed air after each sample measurement to avoid cross-contamination. During exposure to the X-ray beam, the fluid dispenser system via sample syringe oscillates the liquid (aqueous) sample up and down at a typical rate of  $1\text{ }\mu\text{L/sec}$  in order to limit the effects of radiation damage. The SAXS data were collected using a Rayonix MX225-HE CCD detector (pixel size,  $73.2\text{ }\mu\text{m}$ ) at the sample-to-detector distance of  $1.10$  m (covering the scattering vector range of  $0.01$ - $0.75\text{\AA}^{-1}$ ). Each sample was exposed 50 times to the X-ray beam for 2 sec (for the total exposure time of 100 sec). The two-dimensional SAXS powder patterns were processed with the SasTool program<sup>53</sup> in batch mode to radially integrate the intensity and generate averaged one-dimensional intensity ( $I$ ) vs. scattering vector ( $q$ ) profiles. In order to account for background scattering, scattering from capillary and from water buffer, the scattering intensity from sample solution was subtracted for the scattering intensity measured for the same volume of water buffer.

## Conclusions

In summary, we use a combination of SAXS and STXM to determine atomic level structural ordering in lipid layers adsorbed on the Si NW surface. The data show that Si NWs are coated with a thin, potentially bilayer, lipid structure with thicker, multilayered structures formed in the nodes between touching Si NWs. Our measurements also demonstrate that STXM provides the capability to resolve angular dependence in specific bonds within the lipids that compose these thin structures. It is demonstrated that the C=C bond has a more upright than prostrate orientation with respect to the Si surface, which is consistent with prior MD simulations and NMR/infrared spectroscopy studies, and that any tilt away from the surface normal is predominantly in a direction perpendicular to the long axis of the NW. Neither the C=O, nor C-C bonds of the DOPC lipids exhibit comparable angular dependence.

## Acknowledgements

This work was performed under the auspices of the U.S. Department of Energy (DoE), Office of Basic Energy Sciences, Division of Materials Science and Engineering by Lawrence Livermore National Laboratory under Contract No. DE-AC52-07NA27344. The Advanced Light Source is supported by the Director, Office of Science, OBES, of the U.S. DoE under Contract No. DE-AC02-05CH11231. SAXS experiments were carried out at the Stanford Synchrotron Radiation Lightsource (SSRL), a Directorate of SLAC National Accelerator Laboratory and an Office of Science User Facility operated for the US DoE Office of Science by Stanford University. The SSRL Structural Molecular Biology Program is supported by the DoE Office of Biological and Environmental Research, and by the National Institutes of Health, National Center for Research Resources, Biomedical Technology Program (5 P41 RR001209). The authors thank the ALS and SSRL staff for their assistance during the course of these experiments. LLNL-JRNL-663215

## Notes and references

<sup>a</sup> Physical and Life Sciences Directorate, Lawrence Livermore National Laboratory, Livermore, California 94550, United States.

<sup>b</sup> Mechanical Engineering Department, University of California, Berkeley, CA 94720, United States.

<sup>c</sup> The Molecular Foundry, Lawrence Berkeley National Laboratory, Berkeley, CA 94720, United States.

<sup>d</sup> Advanced Light Source Division, Lawrence Berkeley National Laboratory, Berkeley, CA 94720, United States.

\* Email: vanbuuren1@llnl.gov

Electronic Supplementary Information (ESI) available: Details of the building block model used to generate theoretical resonance intensity ratios, discussion of beam damage, details of the method used to determine relative DOPC layer thicknesses, relative intensity maps for data collected across the Si and C K-edges. See DOI: 10.1039/b000000x/

1. L.-Q. Wu and G. F. Payne, *Trends in Biotechnology*, 2004, **22**, 593-599.
2. A. Noy, *Adv. Mater.*, 2011, **23**, 799-799.
3. G. Zheng, F. Patolsky, Y. Cui, W. U. Wang and C. M. Lieber, *Nat Biotech*, 2005, **23**, 1294-1301.

4. F. Patolsky, B. P. Timko, G. Yu, Y. Fang, A. B. Greytak, G. Zheng and C. M. Lieber, *Science*, 2006, **313**, 1100-1104.
5. A. B. Artyukhin, A. Shestakov, J. Harper, O. Bakajin, P. Stroeve and A. Noy, *Journal of the American Chemical Society*, 2005, **127**, 7538-7542.
6. S.-C. J. Huang, A. B. Artyukhin, J. A. Martinez, D. J. Sirbully, Y. Wang, J.-W. Ju, P. Stroeve and A. Noy, *Nano Letters*, 2007, **7**, 3355-3359.
7. J. A. Martinez, N. Misra, Y. Wang, P. Stroeve, C. P. Grigoropoulos and A. Noy, *Nano Letters*, 2009, **9**, 1121-1126.
8. N. Misra, J. A. Martinez, S.-C. J. Huang, Y. Wang, P. Stroeve, C. P. Grigoropoulos and A. Noy, *Proceedings of the National Academy of Sciences*, 2009, **106**, 13780-13784.
9. A. P. Hitchcock, J. J. Dynes, G. Johansson, J. Wang and G. Botton, *Micron*, 2008, **39**, 311-319.
10. J. R. Lawrence, G. D. W. Swerhone, G. G. Leppard, T. Araki, X. Zhang, M. M. West and A. P. Hitchcock, *Appl. Environ. Microbiol.*, 2003, **69**, 5543-5554.
11. D. H. Cruz, M. E. Rousseau, M. M. West, M. Pezolet and A. P. Hitchcock, *Biomacromolecules*, 2006, **7**, 836-843.
12. D. Hernandez-Cruz, A. P. Hitchcock, T. Tyliczszak, M. E. Rousseau and M. Pezolet, *Review of Scientific Instruments*, 2007, **78**.
13. M. E. Rousseau, D. H. Cruz, M. M. West, A. P. Hitchcock and M. Pezolet, *Journal of the American Chemical Society*, 2007, **129**, 3897-3905.
14. J. Stohr, *NEXAFS Spectroscopy*, Springer, 1992.
15. J. Stohr and D. A. Outka, *Physical Review B*, 1987, **36**, 7891-7905.
16. Z. Zhang, S. Y. Bhide and M. L. Berkowitz, *Journal of Physical Chemistry B*, 2007, **111**, 12888-12897.
17. F. A. Nezil and M. Bloom, *Biophysical Journal*, 1992, **61**, 1176-1183.
18. J. B. Klauda, R. M. Venable, J. A. Freites, J. W. O'Connor, D. J. Tobias, C. Mondragon-Ramirez, I. Vorobyov, A. D. MacKerell and R. W. Pastor, *Journal of Physical Chemistry B*, 2010, **114**, 7830-7843.
19. G. Khelashvili, G. Pabst and D. Harries, *Journal of Physical Chemistry B*, 2010, **114**, 7524-7534.
20. G. Khelashvili and D. Harries, *Journal of Physical Chemistry B*, 2013, **117**, 2411-2421.
21. J. P. M. Jambeck and A. P. Lyubartsev, *Journal of Chemical Theory and Computation*, 2012, **8**, 2938-2948.
22. G. Khelashvili, N. Johner, G. Zhao, D. Harries and H. L. Scott, *Chemistry and Physics of Lipids*, 2014, **178**, 18-26.
23. T. J. Piggot, A. Pineiro and S. Khalid, *Journal of Chemical Theory and Computation*, 2012, **8**, 4593-4609.
24. J. Aittoniemi, T. Rog, P. Niemela, M. Pasenkiewicz-Gierula, M. Karttunen and I. Vattulainen, *Journal of Physical Chemistry B*, 2006, **110**, 25562-25564.
25. A. L. Rabinovich, P. O. Ripatti and N. K. Balabaev, *Journal of Biological Physics*, 1999, **25**, 245-262.
26. A. L. Rabinovich, P. O. Ripatti, N. K. Balabaev and F. A. M. Leermakers, *Physical Review E*, 2003, **67**.
27. A. Seelig and J. Seelig, *Biochemistry*, 1977, **16**, 45-50.
28. H. U. Gally, G. Pluschke, P. Overath and J. Seelig, *Biochemistry*, 1979, **18**, 5605-5610.
29. J. Seelig and N. Waespesarcevic, *Biochemistry*, 1978, **17**, 3310-3315.
30. D. E. Warschawski and P. F. Devaux, *European Biophysics Journal with Biophysics Letters*, 2005, **34**, 987-996.
31. I. C. Tran, R. Tunuguntla, K. Kim, T. M. Willey, J. R. I. Lee, M. Bagge-Hansen, A. Noy and T. van Buuren, *In Preparation*, 2014.
32. J. F. Nagle and S. Tristram-Nagle, *Current Opinion in Structural Biology*, 2000, **10**, 474-480.
33. N. Kucerka, J. Pencer, J. N. Sachs, J. F. Nagle and J. Katsaras, *Langmuir*, 2007, **23**, 1292-1299.
34. B. L. Henke, E. M. Gullikson and J. C. Davis, *Atomic Data and Nuclear Data Tables*, 1993, **54**, 181-342.
35. J. H. Hubbell, W. J. Veigele, E. A. Briggs, R. T. Brown, D. T. Cromer and R. J. Howerton, *Journal of Physical and Chemical Reference Data*, 1975, **4**, 471-538.
36. J. H. Hubbell, W. J. Veigele, E. A. Briggs, R. T. Brown, D. T. Cromer and R. J. Howerton, *Journal of Physical and Chemical Reference Data*, 1977, **6**, 615-616.
37. E. Novakova, G. Mitrea, C. Peth, J. Thieme, K. Mann and T. Salditt, *Biointerphases*, 2008, **3**, FB44-FB54.
38. J. R. Lawrence, G. D. W. Swerhone, G. G. Leppard, T. Araki, X. Zhang, M. M. West and A. P. Hitchcock, *Applied and Environmental Microbiology*, 2003, **69**, 5543-5554.
39. B. O. Leung, A. P. Hitchcock, A. Won, A. Ianoul and A. Scholl, *European Biophysics Journal with Biophysics Letters*, 2011, **40**, 805-810.
40. X. R. Liu, K. Eusterhues, J. Thieme, V. Ciobota, C. Hoschen, C. W. Mueller, K. Kusel, I. Kogel-Knabner, P. Rosch, J. Popp and K. U. Totsche, *Environmental Science & Technology*, 2013, **47**, 3158-3166.
41. J. Stewart-Ornstein, A. P. Hitchcock, D. H. Cruz, P. Henklein, J. Overhage, K. Hilpert, J. D. Hale and R. E. W. Hancock, *Journal of Physical Chemistry B*, 2007, **111**, 7691-7699.
42. J. J. Dynes, J. R. Lawrence, D. R. Korber, G. D. W. Swerhone, G. G. Leppard and A. P. Hitchcock, *Science of the Total Environment*, 2006, **369**, 369-383.
43. B. Watts and H. Ade, *Journal of Electron Spectroscopy and Related Phenomena*, 2008, **162**, 49-55.
44. J. R. I. Lee, T. Y. J. Han, T. M. Willey, D. Wang, R. W. Meulenberg, J. Nilsson, P. M. Dove, L. J. Terminello, T. van Buuren and J. J. De Yoreo, *Journal of the American Chemical Society*, 2007, **129**, 10370-10381.
45. T. M. Willey, J. R. I. Lee, J. D. Fabbri, D. Wang, M. H. Nielsen, J. C. Randel, P. R. Schreiner, A. A. Fokin, B. A. Tkachenko, N. A. Fokina, J. E. P. Dahl, R. M. K. Carlson, L. J. Terminello, N. A. Melosh and T. van Buuren, *Journal of Electron Spectroscopy and Related Phenomena*, 2009, **172**, 69-77.
46. J. Wang, G. A. Button, M. M. West and A. P. Hitchcock, *Journal of Physical Chemistry B*, 2009, **113**, 1869-1876.
47. J. Wang, C. Morin, L. Li, A. P. Hitchcock, A. Scholl and A. Doran, *Journal of Electron Spectroscopy and Related Phenomena*, 2009, **170**, 25-36.
48. L. Netzer, R. Iscovici and J. Sagiv, *Thin Solid Films*, 1983, **100**, 67-76.
49. J. R. I. Lee, R. L. O'Malley, T. J. O'Connell, A. Vollmer and T. Rayment, *Journal of Physical Chemistry C*, 2009, **113**, 12260-12271.
50. D. Oyamatsu, S. Kuwabata and H. Yoneyama, *Journal of Electroanalytical Chemistry*, 1999, **473**, 59-67.

51. A. L. D. Kilcoyne, T. Tyliczszak, W. F. Steele, S. Fakra, P. Hitchcock, K. Franck, E. Anderson, B. Harteneck, E. G. Rightor, G. E. Mitchell, A. P. Hitchcock, L. Yang, T. Warwick and H. Ade, *Journal of Synchrotron Radiation*, 2003, **10**, 125-136.
52. A. Martel, P. Liu, T. M. Weiss, M. Niebuhr and H. Tsuruta, *Journal of Synchrotron Radiation*, 2012, **19**, 431-434.
53. SSRL. <<http://ssrl.slac.stanford.edu/~saxs/analysis/sastool.htm>>.